ADVANCES IN MATERIALS SCIENCE, Vol. 25, No. 3 (85), September 2025

DOI: 10.2478/adms-2025-0017

**Justyna Zygmuntowicz[1,*], Joanna Tańska[2], Paulina Wiecińska[2], Paulina Piotrkiewicz[1], Katarzyna Konopka[1], Mikołaj Szafran[2], Marcin Wachowski[3], Ireneusz Szachogłuchowicz[3], Bartosz Michalski[1], Waldemar Kaszuwara[1]**

[1] *Warsaw University of Technology, Faculty of Materials Science and Engineering, Warsaw, Poland*
[2] *Faculty of Chemistry, Warsaw University of Technology, Warsaw, Poland*
[3] *Military University of Technology, Faculty of Mechanical Engineering, Warsaw, Poland*

* *justyna.zygmuntowicz@pw.edu.pl*

# CENTRIFUGAL GEL CASTING OF GRADED $Al_2O_3$-Ni COMPOSITES USING 2-CARBOXYETHYL ACRYLATE

## ABSTRACT

This study presents the fabrication and characterization of functionally graded $Al_2O_3$-Ni ceramic-metal composites using centrifugal gel casting with 2-carboxyethyl acrylate (CEA) as the monomer. Two Series of composites were produced under different centrifugal conditions to investigate their influence on nickel distribution, microstructure, and mechanical performance. The CEA-based gel system enabled the formation of dense green bodies with improved phase dispersion and sintering behavior. Microstructural analysis revealed that lower rotational speed and longer casting time (2500 rpm, 110 min) led to a more uniform radial distribution of nickel particles and reduced agglomeration. This microstructural improvement resulted in significantly higher compressive strength (1620 kN) compared to the faster cast series (977 kN). Digital image correlation confirmed more distributed strain fields and delayed fracture in the optimized samples. These findings demonstrate that casting parameters and monomer chemistry can be effectively tailored to engineer dense, robust, and gradient-structured ceramic–metal composites for high-performance applications.

***Keywords:*** *Functionally graded materials; $Al_2O_3$-Ni composites; centrifugal gel casting; 2-carboxyethyl acrylate; ceramic–metal composites*

## INTRODUCTION

The safe and efficient transport of chemically aggressive fluids, particularly at elevated temperatures, is a critical challenge in advanced industrial processes such as chemical synthesis, waste treatment, and high-temperature catalysis [1-4]. In such demanding environments, conventional metallic or polymeric piping systems often fall short, either due to corrosion, thermal degradation, or mechanical failure [5-7]. The demanding service conditions involving thermal and chemical gradients, which induce complex stress fields and dynamic mechanical loading, have spurred the search for materials that combine chemical inertness, thermal stability, abrasion resistance, and mechanical robustness.

Among advanced ceramics, aluminum oxide stands out as a leading candidate for constructing corrosion-resistant conduits, catalytic reactor linings, and structural elements exposed to aggressive environments [8-10]. Its remarkable chemical inertness across a wide pH range, excellent high-temperature stability, and high hardness make it well-suited for such applications [11-12]. Moreover, $Al_2O_3$ demonstrates outstanding resistance to creep, erosion,

*Received: 16.06.2025; Received in revised form: 02.09.2025; Accepted: 06.09.2025*

and wear, and it remains one of the most commercially viable technical ceramics due to its cost-effectiveness and availability [13-17]. The development of advanced forming techniques such as slip casting, gel casting, and centrifugal forming has further enabled the fabrication of complex-shaped ceramic components, including tubes and hollow bodies, with high dimensional precision and near-net-shape characteristics [18].

However, despite these significant advantages, monolithic alumina components remain inherently brittle, with low fracture toughness and limited resistance to thermal shock. These limitations restrict their use in dynamic or structurally demanding conditions, such as mechanically loaded pipelines or reactors experiencing rapid temperature fluctuations [19-21]. One of the most promising strategies to mitigate this brittleness is the incorporation of a ductile metallic phase into the ceramic matrix to create ceramic–metal composites, also referred to as cermets [22-23]. The inclusion of metals such as nickel offers multiple benefits: metallic particles can arrest or deflect crack propagation, bridge microcracks, and dissipate fracture energy, thereby enhancing overall mechanical toughness while preserving thermal and chemical resistance [24-25].

Beyond simple two-phase mixtures, functionally graded materials (FGMs) have emerged as a particularly attractive solution for applications that involve multi-axial stress states and thermal gradients [26-28]. By gradually varying the composition across the thickness of a component, such as enriching the outer layer with metal to absorb mechanical loads while maintaining a pure ceramic inner layer for chemical durability, FGMs allow for tailored properties that adapt to local operating conditions [29-30]. This gradation not only improves interfacial stress distribution and thermal compatibility between phases but also reduces the likelihood of abrupt failure at interfaces.

Centrifugal forming methods offer unique advantages to achieve such tailored microstructures. By harnessing centrifugal force during solidification, these methods enable the controlled redistribution of particles based on density, facilitating the formation of gradient architectures in ceramic–metal composites. However, successful implementation requires careful control over suspension stability, gelation kinetics, and sintering behavior, all of which depend significantly on the chemistry of the casting medium.

In particular, functionally graded materials offer a solution for optimizing the performance of ceramic–metal components [31-32], by engineering a gradual variation in composition across the pipe wall such that the inner layer remains pure $Al_2O_3$ for maximum chemical resistance. At the same time, the outer surface is enriched with metal particles to enhance toughness; the material can be tailored to withstand complex, multidirectional stresses [18, 21, 34]. The graded structure also enables a smooth transition in thermal and elastic properties, mitigating internal stresses caused by thermal expansion mismatch and reducing the likelihood of catastrophic failure.

Moreover, recent studies on advanced hybrid and nanostructured materials have emphasized the importance of tailored phase distribution and interfacial compatibility in enhancing mechanical and thermal performance. In particular, Kausar and co-workers have demonstrated how the controlled design of nanocomposite architectures through selection of matrix composition and dispersion strategy can lead to improved strength, thermal stability, and functional properties in high-performance polymer and hybrid systems [34]. These insights offer valuable parallels for ceramic–metal composites, where microstructural gradation and phase integration are critical to achieving multifunctionality.

In this context, our work introduces a novel approach that combines centrifugal gel casting with 2-carboxyethyl acrylate (CEA**)** as a polymerizable monomer to fabricate graded $Al_2O_3$-Ni composites. CEA offers improved slurry stability and cleaner burnout compared to conventional acrylamide systems, contributing to denser, more uniform green bodies. By systematically varying centrifugal casting parameters, namely speed and time, we evaluate their effect on the radial distribution of nickel particles, microstructural uniformity, and compressive strength. This dual optimization of chemical formulation and processing dynamics allows us to engineer functionally graded structures with enhanced mechanical integrity, providing a promising pathway for the design of robust ceramic–metal components intended for chemically aggressive and thermally challenging environments.

It should be emphasized that the novelty of this study lies in the synergistic use of centrifugal gel casting and 2-carboxyethyl acrylate monomer chemistry to fabricate functionally graded $Al_2O_3$-Ni composites with enhanced phase uniformity and mechanical performance. While centrifugal techniques have previously been explored for gradient material formation, the application of CEA, a monomer offering both strong dispersion stability and efficient polymerization in aqueous systems, has not been systematically examined in this context. Unlike conventional acrylamide-based systems, CEA improves slurry homogeneity, reduces agglomeration of the metallic phase, and facilitates clean burnout during sintering. Moreover, by precisely adjusting centrifugal casting parameters (speed and time), we demonstrate the ability to control nickel particle migration and distribution across the ceramic matrix, resulting in highly dense and mechanically robust composites. This dual optimization of material chemistry and casting dynamics provides a new route for tailoring microstructure–property relationships in ceramic metal systems, particularly for applications requiring high thermal and mechanical resilience.

## MATERIALS AND METHODS

For the preparation of the composite suspensions, $\alpha$-$Al_2O_3$ ceramic powder (TM-DAR grade, Taimei Chemicals, Japan) was employed as the ceramic matrix. Nickel powder (Sigma-Aldrich) served as the metallic phase component. The polymerization system was based on 2-carboxyethyl acrylate (CEA, Sigma-Aldrich), which acted as the monomer. Diammonium hydrogen citrate (DAC, POCH, analytical grade) was utilized as a dispersant to stabilize the suspension. Ammonium persulfate ($(NH_4)_2S_2O_8$, Sigma-Aldrich, 98%) in the form of a 5% aqueous solution was applied as the polymerization initiator. All suspensions were prepared using distilled water as the solvent.

$Al_2O_3$-Ni composite samples were prepared using the centrifugal gel casting method. Two Series of samples (Series A and Series B) were fabricated using identical compositions but subjected to different centrifugal casting parameters to evaluate the influence on microstructure development and selected properties. Both slurries used to produce the samples contained 50% by volume of the solid phase, including 10% by volume of the metallic phase in the form of nickel.

The starting suspensions were prepared by dispersing $Al_2O_3$ powder and nickel powder in deionized water with the addition of diammonium hydrogen citrate (DAC) as a dispersant and N,N,N',N'-tetramethylethylenediamine (TEMED) as a polymerization accelerator. The proportion of TEMED in relation to the monomer (TEMED was in the form of a 10% solution) was 1% by weight. 2-Carboxyethyl acrylate (CEA) was used as a monomer to facilitate in situ polymerization during casting. The monomer content in relation to dry mass was 5% by weight. The slurries were mixed using a high-speed homogenizer (Thinky ARE-250) in a three-step process: initial mixing for 8 minutes at 800 rpm, deaeration for 2 minutes at 1800 rpm, followed by an additional mixing step for 3 minutes at 800 rpm.

After homogenization, ammonium persulfate was added as a polymerization initiator. The proportion of APS (ammonium persulfate) initiator relative to the monomer (the initiator was in the form of a 5% solution) was 5% by weight. The slurries were then mixed again in the Thinky ARE-250 device for 30 seconds at 800 rpm to ensure uniform distribution of the initiator.

The final slurries were subjected to centrifugal gel casting under distinct conditions for each Series. For Series I, the slurry was centrifuged for 60 minutes at a rotational speed of 3000 rpm. In contrast, Series II samples were cast for 110 minutes at 2500 rpm. These parameters were selected to influence particle redistribution and alignment during solidification, with the aim of tailoring the resulting composite microstructure. The process diagram is shown in Figure 1.

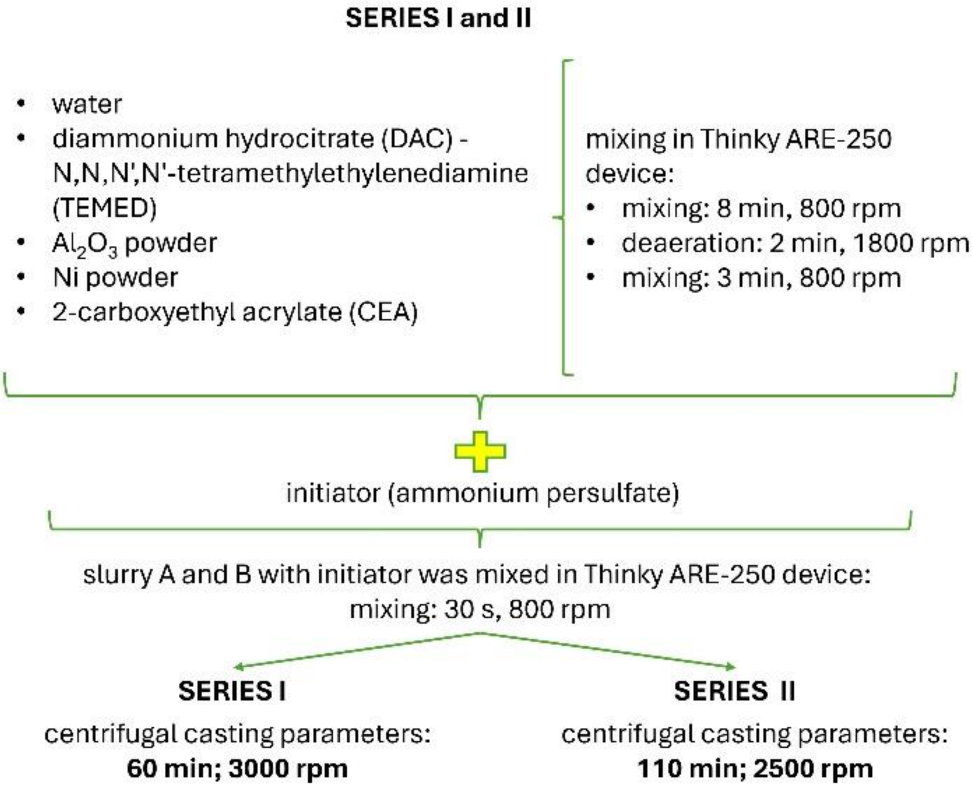


**Fig. 1.** Schematic diagram of the sample preparation procedure for Series I and II using the centrifugal gel casting method

The physical properties of the sintered composite samples were evaluated in accordance with the PN-76/E-06307 standard, employing the Archimedes principle [35]. This method is based on the determination of density through buoyancy measurements, whereby each sample is first weighed in air and subsequently immersed in a liquid of known density. The difference in mass allows for the calculation of the sample's volume, enabling the determination of both apparent density and open porosity. This approach provides precise and reproducible measurements, which are critical for assessing the structural integrity and performance of ceramic–metal composites. In addition to density and porosity measurements, dimensional analysis was conducted to evaluate the linear and volumetric shrinkage of the samples resulting from the sintering process. These measurements provide insight into the extent of densification and the dimensional stability of the ceramic–metal composite.

Phase composition analysis is essential for understanding and optimizing the properties of ceramic–metal composites for targeted applications. In this study, X-ray diffraction (XRD) was employed to characterize the phase assemblages present in the composites both prior to and following the sintering process. The analyses were carried out using a Rigaku Miniflex II diffractometer equipped with a copper X-ray source (λ = 1.54059 Å). Scans were conducted over a 2θ range of 20–100°, with a step size of 0.01° and a counting time of 2 seconds per step, ensuring the acquisition of high-resolution diffraction patterns suitable for detailed phase evaluation. Phase identification was performed using MDI Jade 8.8 software in conjunction with the ICDD PDF-4+ 2023 database, enabling precise matching of observed diffraction peaks to known crystallographic standards. Comparative analysis of the green and sintered states revealed notable differences in phase composition, reflecting structural transformations induced by the sintering process. These findings offer valuable insights into phase evolution and material stability, contributing to the informed design and processing of ceramic–metal composites.

Microstructural characterization of the ceramic–metal composites was carried out using scanning electron microscopy (SEM). To enable detailed observation, the sintered samples—fabricated in a tubular geometry—were sectioned into 1 cm or 1.5 cm-high segments taken from the central region of each specimen. These segments were mounted in conductive resin using a hot-mounting technique to ensure stability and conductivity during imaging. Standard metallographic procedures, including sequential grinding and polishing, were employed to prepare high-quality cross-sections for microscopic examination. SEM analyses were performed using a JEOL JSM-6610 microscope operated at an accelerating voltage of 15 kV, providing high-resolution imaging of the composite microstructure. This approach facilitated reliable visualization of the metallic phase distribution within the ceramic matrix, enabling accurate assessment of the sintered composites. To evaluate the radial distribution of elements within the composite cross-sections, energy-dispersive X-ray spectroscopy (EDX) line analysis was performed across the wall thickness of sintered samples from Series I and Series II.

Evaluating the compressive strength of composite materials is essential for assessing their suitability in structural and engineering applications. In this study, the mechanical response of sintered ceramic–metal composites, shaped into hollow cylindrical specimens, was investigated under monotonic compression. Testing was conducted in accordance with the ISO 2739:2010 (EN) standard, using an Instron 8802 MT hydraulic testing system. This apparatus, equipped with dedicated software, enabled continuous acquisition of load versus displacement data during the compression process. To enhance the resolution of deformation analysis, a digital image correlation (DIC) system was employed for real-time mapping of surface strain fields. This non-contact optical method provided detailed insight into the local deformation behavior and crack initiation zones. A high-speed camera was used concurrently to capture visual evidence of failure onset, allowing for correlation between mechanical data and crack propagation events. Failure was defined by the appearance of a sharp decline in the load-displacement curve, corresponding to the formation of visible cracks. The integration of mechanical testing with DIC and high-speed imaging offered a comprehensive assessment of the material's deformation mechanisms and failure behavior, contributing to a deeper understanding of the structural performance of ceramic–metal composites under compressive loading.

The microstructural characteristics of ceramic–metal composites, particularly the grain size of the alumina matrix, play a critical role in determining their mechanical performance. In this study, quantitative image analysis was employed to assess the influence of process parameters on alumina grain growth following sintering. Representative micrographs were obtained from randomly selected areas of the composite samples, with each image containing at least 300 alumina grains. Image analysis was carried out using the "MicroMeter" software [36-39], which enabled automated and reproducible quantification of microstructural features. The original grayscale images were subjected to binarization by applying a threshold, allowing for the clear separation of the metallic and ceramic phases. This binarization process facilitated the determination of alumina grain sizes. The grain size data were extracted from the binary images using shape and area descriptors, ensuring consistency across multiple sample regions. The resulting measurements enabled statistical evaluation of the grain size distribution of the sintered composites.

## RESULTS AND DISCUSSION

Figure 2 shows sintered $Al_2O_3$-Ni composite samples obtained via centrifugal gel casting: (a) Series I and (b) Series II. Each subfigure presents both the front and side views of the hollow cylindrical samples. The samples in Series I, centrifuged at 3000 rpm for 60 minutes, exhibit a visibly rougher internal surface and less uniform wall thickness, indicating inhomogeneous particle distribution during solidification. In contrast, the Series II samples, cast at a lower speed of 2500 rpm for a longer duration (110 minutes), show a smoother and more uniform inner surface and consistent wall geometry. These differences highlight the significant influence of centrifugal casting parameters on the microstructural integrity and morphological uniformity of the final sintered bodies. Scale bars represent 1 cm.

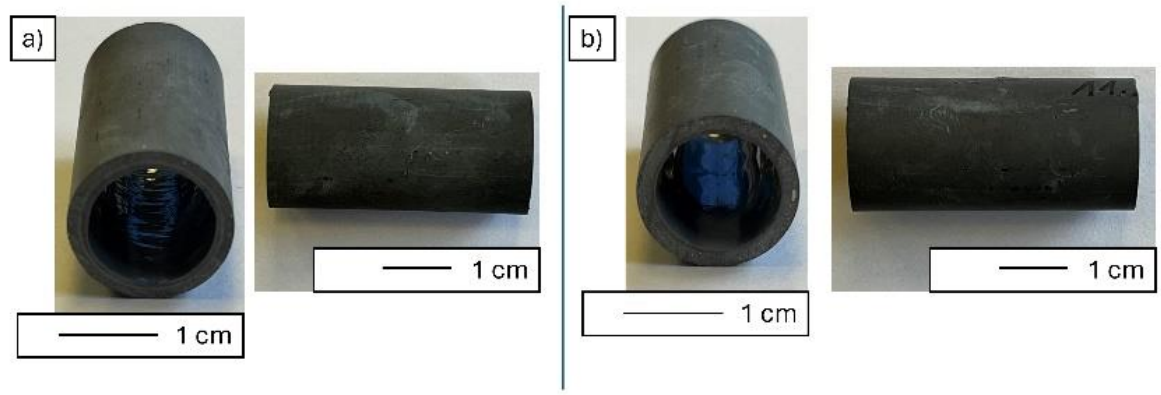


**Fig. 2.** Photos of sintered Al2O3-Ni composite samples prepared by centrifugal gel casting under different processing conditions: a) Series I, b) Series II

The relative density for Series I was 99.03 ± 0.24%, while for Series II it was equal to 98.37 ± 1.05%. The open porosity for Series I was determined at the level of 3.93 ± 0.48%, while for Series II, it was the value of 3.75 ± 0.70%. The water absorption for the composites produced in the case of Series I was equal to 0.94 ± 0.11%, while for Series II it was equal to 0.90 ± 0.17%.

The linear shrinkage measured after the height for Series I was equal to 13.55 ± 0.02%, while for Series II it was the value of 14.21 ± 0.21%. Whereas the linear shrinkage measured in diameter for Series I was equal to 13.56 ± 0.12%, and for Series II it was equal to 14.24 ± 0.17%. The volumetric shrinkage for Series I was 28.23 ± 0.23%, while for Series II it was determined at 37.27 ± 0.38%.

An important aspect influencing the quality and performance of ceramic–metal composites fabricated via gel-casting is the selection of the monomer. In the present study, 2-carboxyethyl acrylate (CEA) was employed as the monomer for in situ polymerization during centrifugal gel casting of $Al_2O_3$-Ni composites. This system was compared to the acrylamide-based formulation (acrylamide/MBAM) previously used in a related study by the authors, focused on thermoanalytical analysis of similar composites [18].

CEA is a monofunctional acrylic monomer with a polar carboxylic acid group, which contributes both to the gelation process and to enhanced dispersion of ceramic and metallic powders within the suspension [40]. Its polar –COOH functional group can interact electrostatically with alumina and nickel particle surfaces, thereby improving slurry stability and minimizing agglomeration [40]. In contrast, the acrylamide (AM)-based system requires the addition of a crosslinker, N,N'-methylenebisacrylamide (MBAM), to achieve a three-dimensional gel network, and does not offer the same particle-surface affinity due to the lack of functional anchoring groups [18].

The effectiveness of the CEA-based system is evident in the significantly higher relative density values obtained in this study. Composites fabricated in this investigation, Series I (3000 rpm, 60 min) and Series II (2500 rpm, 110 min), achieved relative densities of 99.03 ± 0.24% and 98.37 ± 1.05%, respectively. These values exceed those reported in the prior work, where relative densities ranged from approximately 98.31 ± 0.53% under similar thermal and sintering conditions. Additionally, the current study showed well-controlled volumetric shrinkage, indicating effective burnout of organics and uniform densification. The improved densification observed in the present work can be attributed to multiple factors: the stabilizing effect of CEA on particle dispersion during gelation, the formation of a homogeneous polymeric matrix that immobilizes the particles during casting, and the clean decomposition profile of CEA during burnout, which minimizes pore formation and residue. In contrast, acrylamide-based gels are known to produce more carbonaceous residue during pyrolysis and may exhibit non-uniform shrinkage if the gel structure is insufficiently crosslinked.

Overall, the choice of CEA as a monomer represents a process optimization that enhances green body integrity, reduces residual porosity after sintering, and supports the formation of structurally homogeneous and mechanically robust $Al_2O_3$-Ni composites. This improvement, combined with the tailored control of centrifugal casting parameters explored in this work, demonstrates a significant advancement over previous studies and establishes a more effective route for forming high-density ceramic–metal components.

The phase composition of the sintered $Al_2O_3$-Ni composites was examined using X-ray diffraction (XRD), and the results are presented in Figure 3. Both Series I and Series II exhibit diffraction patterns characteristic of $\alpha$-$Al_2O_3$ (corundum) as the dominant crystalline phase. The presence of metallic nickel was also confirmed in both Series, although the intensity of its diffraction peaks is noticeably lower, consistent with its lower volumetric fraction (10%). In the diffractogram of Series I (Figure 3a), the Ni peaks are relatively weak and appear primarily at $2\theta$ angles corresponding to the (111), (200), and (220) planes of face-centered cubic (FCC) nickel. The signal-to-noise ratio for Ni reflections is modest, indicating either partial crystallinity or reduced scattering due to limited grain size or distribution heterogeneity.

In contrast, the XRD pattern for Series II (Figure 3 b) reveals slightly more intense and well-defined Ni peaks at similar 2θ positions. The observed microstructural changes suggest improved alignment or redistribution of nickel particles during the centrifugal casting process conducted at 2500 rpm for a longer duration (110 minutes). The sharper and more intense $Al_2O_3$ peaks in Series II also imply better crystallinity and potential grain growth, which is consistent with the SEM and grain size analysis data.

No additional phases such as nickel oxide (NiO) or spinel compounds (e.g., $NiAl_2O_4$) were detected in either Series, indicating that the sintering conditions did not lead to significant interfacial reactions or secondary phase formation. XRD analysis confirms the thermal stability of the composite system and suggests that nickel remained in its metallic state after sintering. Overall, the XRD analysis supports the microstructural observations and confirms the biphasic composition of the composites, with differences in peak sharpness and intensity reflecting subtle microstructural variations induced by the different centrifugal casting parameters.

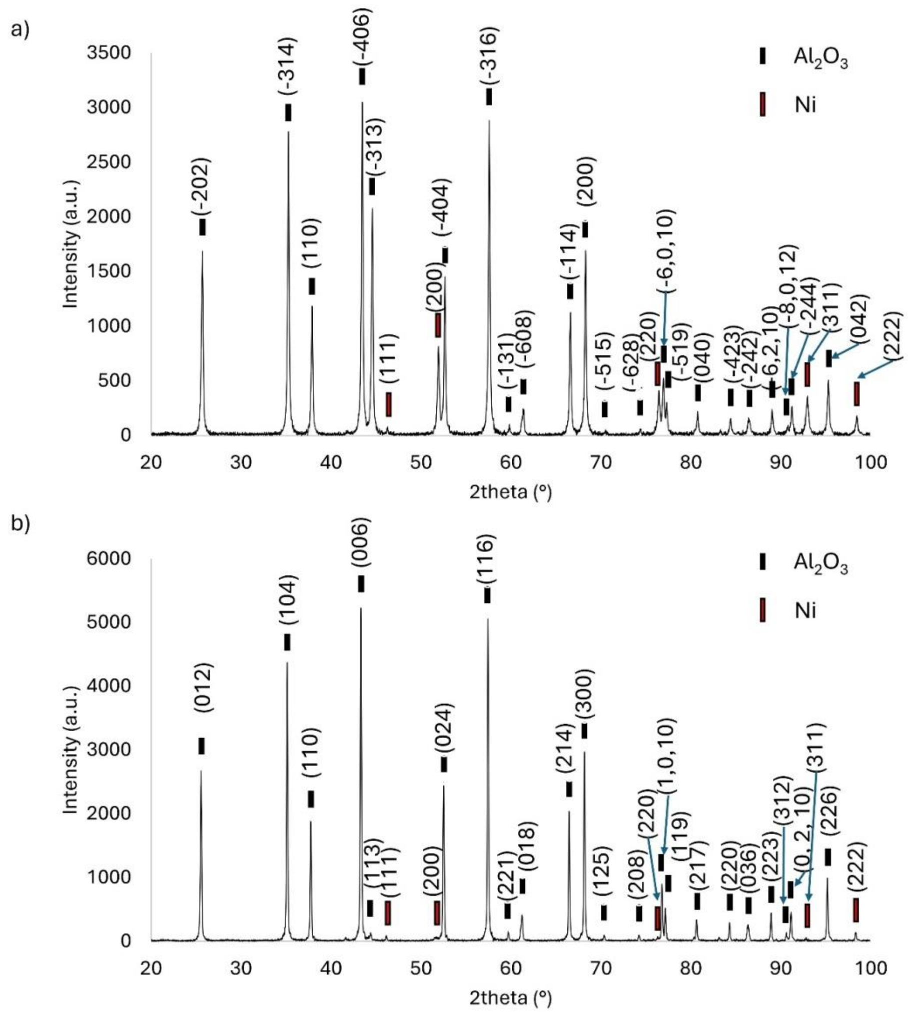


**Fig. 3.** X-ray diffraction (XRD) patterns of sintered Al2O3-Ni composites fabricated via centrifugal gel casting: (a) Series I (3000 rpm, 60 min) and (b) Series II (2500 rpm, 110 min)

Figure 4 presents cross-sectional scanning electron microscopy (SEM) images of sintered $Al_2O_3$-Ni composites obtained via centrifugal gel casting, with distinct microstructural zones identified across the composite wall for two processing conditions: (a) Series I, cast at 3000 rpm for 60 minutes, and (b) Series II, cast at 2500 rpm for 110 minutes. The observed differences in nickel particle distribution reflect the influence of centrifugal casting parameters on the composites. In both Series, the brighter areas correspond to the metallic phase (Ni), while the darker matrix represents alumina ($Al_2O_3$).

In the case of Series I (Figure 4a), three clearly distinguishable zones can be identified across the radial cross-section. Zone I, located closest to the mold wall, exhibits a high concentration of nickel particles. This accumulation results from the high centrifugal force that drives the denser metallic phase outward during casting. However, due to the shorter processing time, the nickel distribution in this zone is somewhat clustered, with visible agglomerates. Zone II, the intermediate region, presents a gradual decline in nickel content with a less uniform distribution, indicating incomplete redistribution and transitional settling of metallic particles. Zone III, positioned nearest the inner surface of the cylindrical sample, is largely devoid of nickel, consisting almost entirely of the alumina matrix. This strongly layered microstructure indicates that the rapid casting at high speed was insufficient for achieving uniform particle dispersion, leading to significant phase segregation.

In contrast, the microstructure of Series II (Figure 4 b) reveals improved homogeneity across all three zones. While Zone I still shows a higher concentration of nickel particles, the distribution is more uniform and less prone to agglomeration compared to Series I. In Zone II, the transition between nickel-rich and nickel-poor areas is smoother, reflecting enhanced redistribution and alignment of particles due to the longer casting time at a lower rotational speed. Notably, Zone III in Series II contains a sparse but visible presence of nickel particles, indicating that the optimized casting parameters allowed some metallic phase to remain within the inner regions of the sample. This more uniform radial distribution of nickel in Series II supports improved structural integration of the metallic and ceramic phases.

Overall, the comparison between the two Series demonstrates that reducing the centrifugal speed and extending the casting duration promotes even dispersion of the nickel phase throughout the ceramic matrix. These microstructural observations are consistent with the mechanical testing results discussed in the next part of the manuscript, where Series II exhibited significantly enhanced compressive strength. The more balanced phase distribution in Series II contributes to superior mechanical performance by minimizing stress concentrations and promoting better load transfer between phases.

The upper panels in Figure 5 display representative backscattered electron (BSE) images with the corresponding scan paths indicated in yellow. In contrast, the lower panels present the EDS intensity profiles (in counts per second, cps) for oxygen (O Kα1), aluminum (Al Kα1), and nickel (Ni Kα1) along the scanned distance. In Series I (Figure 5a), the EDS profile reveals a distinctly layered distribution of the metallic and ceramic phases. The nickel signal (Ni Kα1, blue curve) is prominent in the initial segment of the scan (0–400 μm), corresponding to the outermost region of the cylindrical composite, and gradually diminishes toward the inner wall. This trend confirms the outward migration and accumulation of the denser Ni particles under the high centrifugal force during casting. The steep decline in nickel intensity, coupled with the persistent but fluctuating Al and O signals (red and green curves, respectively), indicates a sharp compositional gradient and partial segregation of the metallic phase. The current findings are consistent with previous SEM observations and confirm the formation of a functionally graded microstructure, albeit with notable heterogeneity in the metallic distribution. In contrast, the EDS line scan for Series II (Figure 5 b) demonstrates a more gradual and uniform distribution of the nickel phase across the wall thickness. Although the nickel signal still shows a higher concentration in the outer region (0–400 μm), it remains detectable throughout a significantly greater portion of the profile. The observed microstructural uniformity suggests that the reduced rotational speed and prolonged casting duration allowed for more effective redistribution of nickel particles prior to gelation. The aluminum and oxygen signals in Series II exhibit reduced fluctuation compared to Series I, reflecting improved microstructural homogeneity and phase continuity.

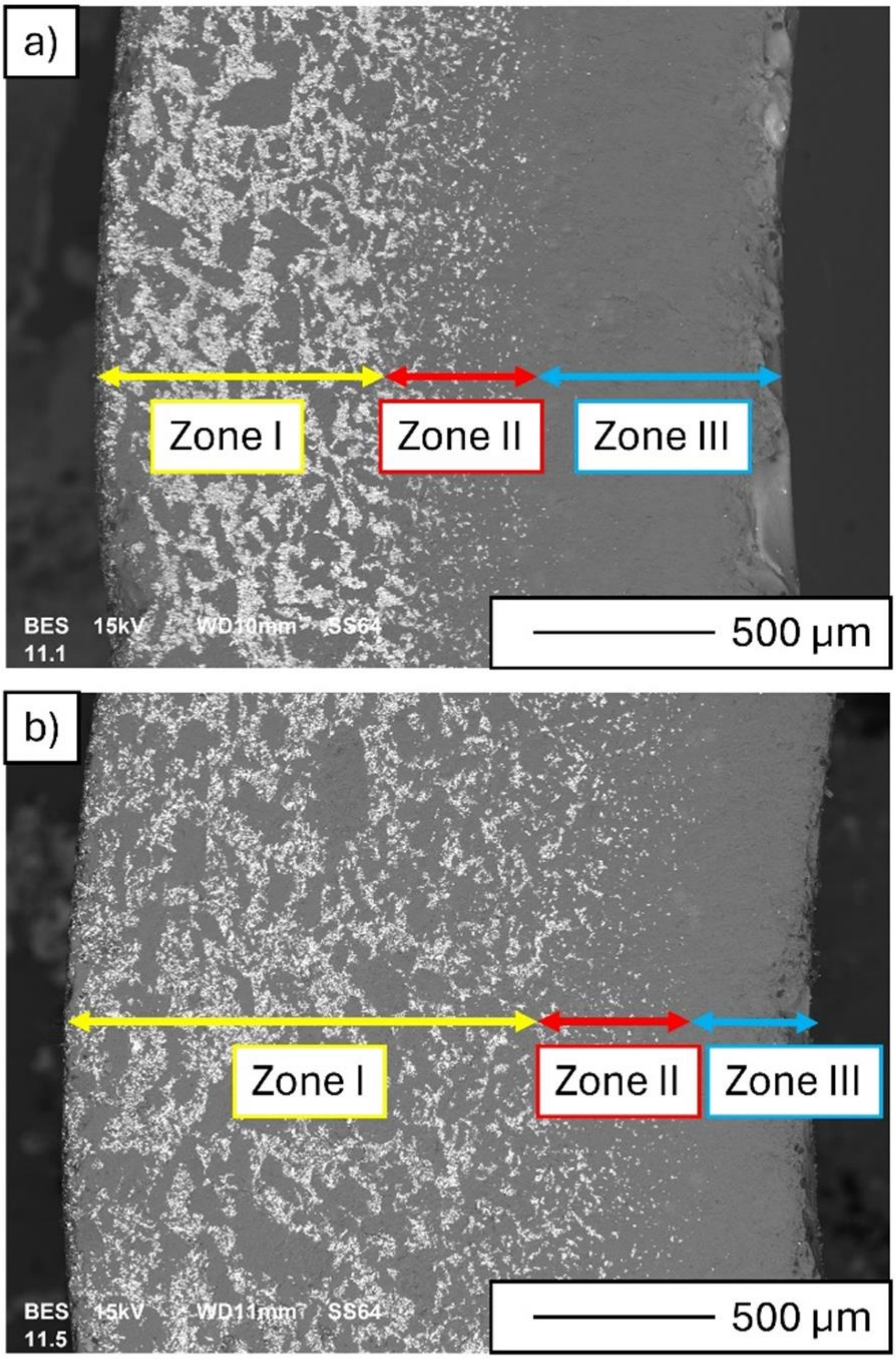


**Fig. 4.** Cross-sectional SEM images of sintered Al2O3-Ni composites fabricated via centrifugal gel casting: (a) Series I (3000 rpm, 60 min) and (b) Series II (2500 rpm, 110 min). Three distinct zones are visible across the wall thickness: Zone I (outer region), Zone II (intermediate region), and Zone III (inner region), differing in the concentration and distribution of nickel particles

The differences in elemental distribution between the two Series directly correlate with their processing parameters. In Series I, the rapid casting at 3000 rpm for 60 minutes limited the time available for particle migration and redistribution, resulting in a highly graded structure with a nickel-depleted inner region. Conversely, in Series II, the lower rotational speed (2500 rpm) and extended casting duration (110 minutes) facilitated a more balanced radial particle distribution, yielding a composite structure with improved metallic phase continuity and reduced gradient sharpness.

These findings further support the SEM-based microstructural analysis and are consistent with the mechanical testing results, wherein Series II exhibited significantly higher compressive strength. The more uniform distribution of the metallic phase likely contributes to enhanced stress transfer and reduced crack initiation sites under mechanical loading.

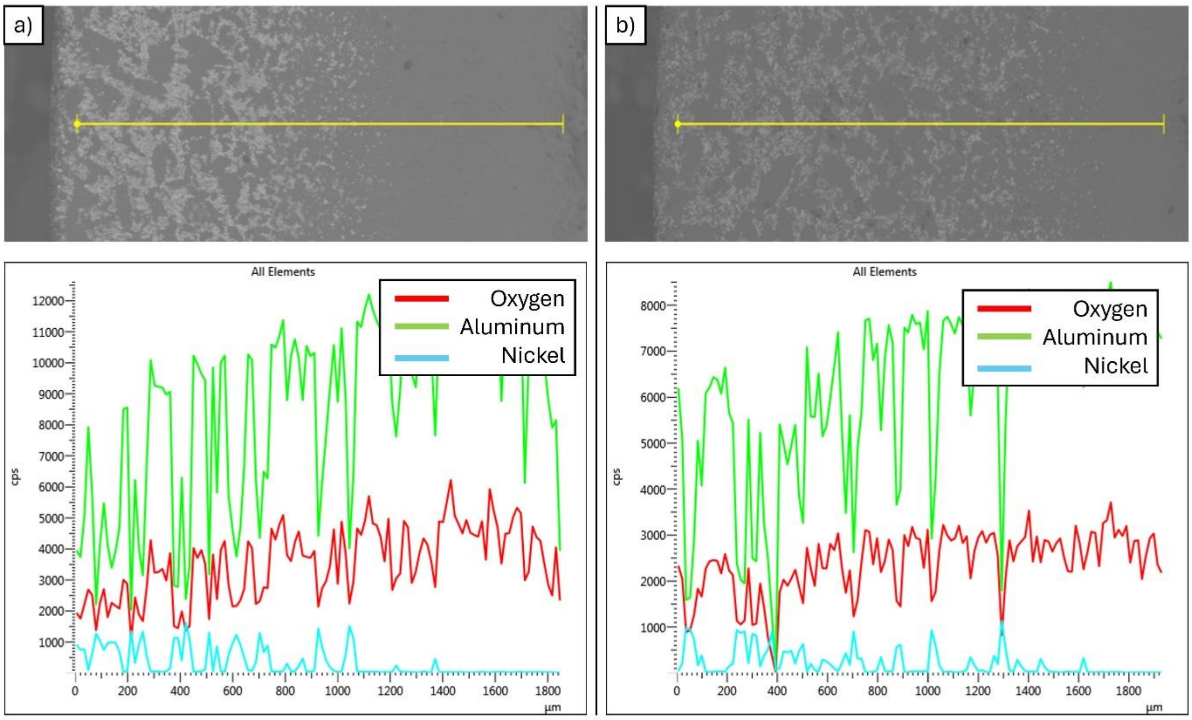


**Fig. 5.** EDS line analysis of Al2O3-Ni composites prepared by centrifugal gel casting: (a) Series I (3000 rpm, 60 min) and (b) Series II (2500 rpm, 110 min)

Figure 6 illustrates the force–displacement curves obtained from compression tests conducted on two composite Series: Series I (represented by the blue line) and Series II (orange line). In both composites, the initial loading response up to failure is predominantly elastic, characterized by a nearly linear increase in force with minimal displacement—indicative of high stiffness. There is no evident plastic deformation stage, as the ceramic-dominated $Al_2O_3$ matrix in these materials leads to brittle failure once a critical load is surpassed. The composite from Series I, centrifuged at 3000 rpm for 60 minutes, reaches a peak load of only around 977.22 kN. In contrast, Series II, cast at a lower speed of 2500 rpm for a 110-minute duration, demonstrates a notably higher compressive strength, reaching about 1620.43 kN. The mechanical test results imply that the composite cast at a lower rotational speed for a longer duration endures significantly greater compressive forces compared to Series I. Additionally, the steeper slope and higher peak of the Series II curve suggest that this material possesses marginally higher stiffness. The gentler slope and lower peak force observed in Series I indicate a more compliant (less stiff) behavior, likely resulting from the higher speed used during the centrifugal casting process. Both composites exhibit elastic behavior until cracking begins—there is no noticeable plastic plateau. Once the maximum load is achieved, failure occurs rapidly. For Series I and II, this is seen as an almost vertical force drop at a displacement of about 0.06 mm (Series I) and 0.15 mm (Series II), reflecting a sudden and catastrophic break. The observed mechanical behavior indicates that the material retains some load-bearing capacity post-crack initiation, suggesting non-brittle failure characteristics. Nonetheless, both composites display minimal plasticity overall; once the peak load is reached, extensive cracking and a sharp drop in load capacity follow.

In contrast, $Al_2O_3$-Ni composites fabricated via centrifugal slip casting (CSC) under a magnetic field, as reported in our previous works [41], exhibited a compressive strength of only 128.9 MPa. Although the CSC approach enabled the alignment of Ni particles under a 450 mT magnetic field, the resulting microstructure displayed anisotropic fracture behavior and earlier failure under load, as evidenced by crack propagation along both vertical and horizontal axes.

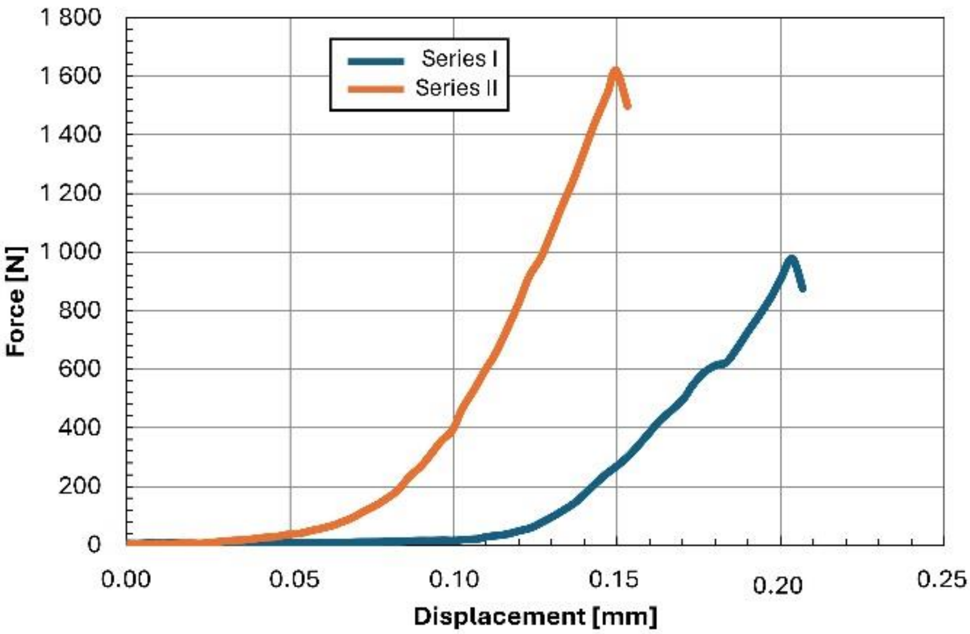


**Fig. 6.** The force–displacement curves obtained from compression tests conducted on two composite Series: Series I (represented by the blue line) and Series II (orange line)

The tests were performed for two ceramic tubes made of $Al_2O_3$-Ni using the centrifugal gel casting method, subjected to a gradually increasing load. The analysis used the Digital Image Correlation (DIC) method, which allows for the observation of displacements. The tests used Istra4D V4.7 x64 devices from Dantec. Figure 7 presents the displacement distributions for the subsequent loading stages.

The results obtained for Series I (Figure 7a) indicate that the initial state, minimal displacements, and an almost uniform distribution. No local strain concentrations. In the next stage, the first zone of increased displacements appears - a potential place of microcrack initiation. Then the growth of the deformation area. Increased displacements located in a narrow strip suggest crack propagation along the vertical axis of the load. One can observe the emerging asymmetry of displacements, the structure of which is continuous in the local area. An increase in the displacement gradient. When approaching the critical level of deformation (just before the crack), the displacements increase rapidly, a crack appears, and the structure is torn. In the last stage, the displacement fields indicate the separation of material fragments.

The results obtained for Series II (Figure 7 b) show that the sample is undeformed. At the initial stage of loading, a local concentration of displacements appears on the sample surface, located asymmetrically, near one of the side edges. The irregularity in the load-displacement curve suggests the presence of local material inhomogeneity or a micro-defect that triggered plastic deformation or micro-crack initiation. Then, during further loading, the area of local displacements expands. Interestingly, a second, independent area of displacement concentration appears - this time on the opposite side of the sample. Both areas show asymmetric deformation distributions. The presence of two distinct load drops in the mechanical response may indicate the existence of two initial structural defects—such as pores, micro-cracks, or variations in material density—that act as competing damage initiation centers. In the next step, two displacement foci develop independently. It is clearly visible that the material does not crack in one central location - instead, a bipolar crack initiation occurs. This phenomenon is unusual for homogeneous materials, but can occur in technical ceramics with non-ideal microstructure. The progressive crack starts to propagate from both sides towards the center of the sample. Areas of high displacement gradient (bright streaks on DIC maps) partially merge, creating a zone of extensive structural instability. In the final stage, the structure is destroyed – the sample separates. The displacement field shows significant displacements in two zones.

The application of Digital Image Correlation in this study enabled a detailed, non-contact analysis of the deformation and failure behavior of $Al_2O_3$-Ni functionally graded composites during monotonic compression. The evolution of displacement fields, as presented in Figure 7, reveals distinct deformation mechanisms between the two sample series. In Series I, a localized zone of vertical displacement developed rapidly, indicating early crack initiation along the loading axis. At the same time, Series II displayed more distributed and asymmetric deformation patterns, with multiple competing damage sites—a feature indicative of enhanced energy absorption and delayed fracture.

These findings are consistent with prior work by Gonzalez et al. [42], who demonstrated that metal-reinforced ceramic composites with graded or non-uniform microstructures exhibit more diffuse strain localization under compressive load, resulting in higher damage tolerance. Similarly, Wu et al. [43] employed DIC to study alumina–metal composites and reported that crack initiation frequently begins at ceramic–metal interfaces with phase discontinuities, a behavior also observed in the displacement gradient maps in the present study.

The current results further reinforce the utility of DIC for analyzing brittle–ductile interactions in ceramic–metal systems. As previously highlighted by Périé et al. [44], DIC offers precise insights into the localization and evolution of strain preceding fracture, especially in functionally graded materials where traditional strain gauges fail to capture local heterogeneities. The successful implementation of DIC in this work provides a deeper understanding of the failure processes in graded $Al_2O_3$-Ni composites. It validates the use of casting time and rotational speed as tunable parameters to control mechanical behavior through microstructural tailoring.

SEM images (Figure 8a, b) display the fracture surfaces of both investigated composite Series. The analysis shows that individual $Al_2O_3$ grains are distinctly visible, typically presenting a roughly equiaxed polyhedral morphology. The clear definition of grain boundaries suggests that cracking primarily occurred along these interfaces, indicating an intergranular fracture mechanism. The grains themselves remain mostly intact, showing no signs of splitting, which further supports the conclusion that the fracture propagated along the grain boundaries rather than through the grains.

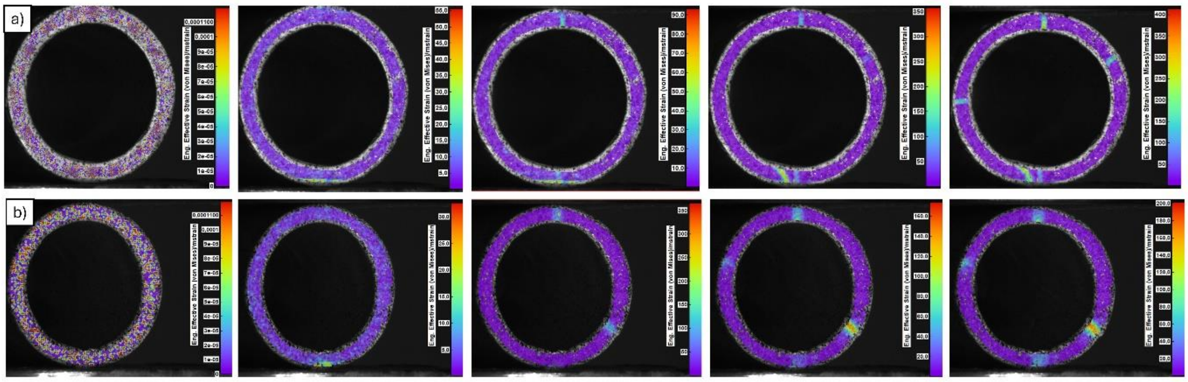


**Fig. 7.** Displacement fields obtained by digital image correlation (DIC): a) Series I, b) Series II

This intergranular fracture mode is evident from the continuous grain-boundary patterns observed on the fracture surfaces. Since grain boundaries are typically the weakest points in such materials, the crack path follows these interfaces. In cases where a ductile Ni phase is present at the boundaries, it may have been dislodged during fracture, possibly leaving small voids or indentations on the surrounding grains. In Series I (Figure 8a), the exposed grains exhibit a uniform and fine-grained structure, generally ranging from 0.5 to 1 µm in size. Most grains are of similar dimensions, indicating a narrow grain size distribution. By comparison, Series II (Figure 8 b) shows a similar grain size distribution with generally larger grains. Some flat, extended grains reach up to one micron in size across, suggesting either larger individual grains or the presence of cleavage planes that span much of a single grain. This variation in grain size points to a coarser microstructure in Series II relative to Series I.

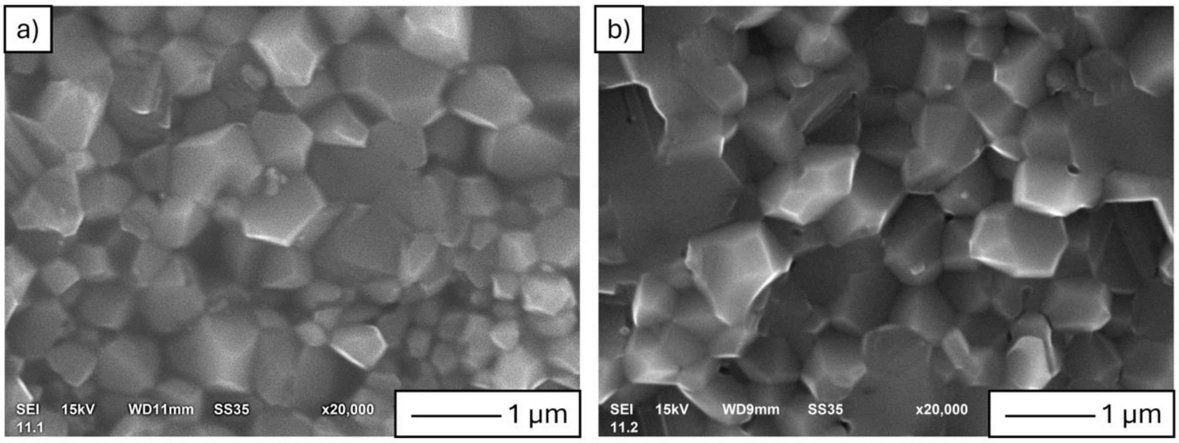


**Fig. 8.** SEM images of the fracture surfaces of the investigated composites: a) Series I, b) Series II

Figure 9 presents the grain size distribution histograms of $Al_2O_3$ particles in the sintered $Al_2O_3$-Ni composites obtained from two different Series: a) Series I and b) Series II. The histograms illustrate the percentage share of grains as a function of the equivalent grain diameter ($d_2$), measured in micrometers (µm).

In both cases, the distributions exhibit a unimodal character, indicating a relatively uniform grain size population. For Series I (Figure 9a), the majority of grains fall within the 0.20–0.60 µm range, with the maximum frequency observed near 0.40 µm. The calculated average grain diameter for this Series is $d_2 = 0.43 \pm 0.21$ µm, reflecting a moderate degree of grain coarsening and a relatively narrow distribution.

In Series II (Figure 9 b), the grain size distribution appears slightly broader and is shifted marginally toward larger diameters. The highest frequency of grains also centers around 0.40–

0.50 µm, but the presence of grains above 1.0 µm is more pronounced compared to Series I. The average grain diameter increases slightly to $d_2 = 0.46 \pm 0.24$ µm, suggesting a minor but noticeable growth of $Al_2O_3$ grains in this Series.

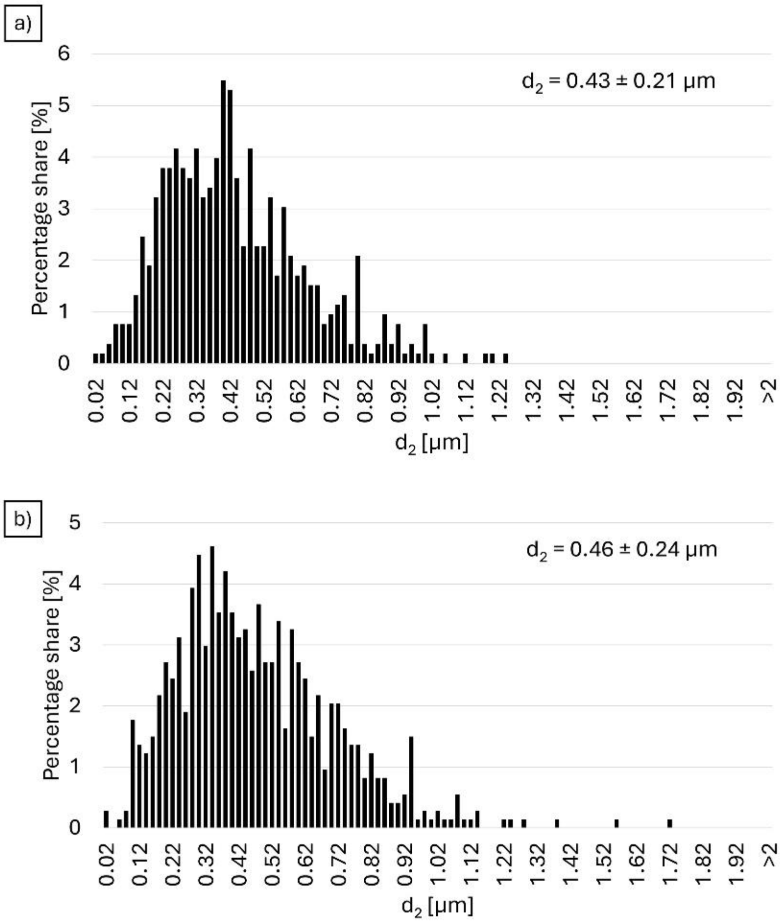


**Fig. 9.** Grain size distribution ($d_2$) of $Al_2O_3$ particles in sintered $Al_2O_3$-Ni composites: a) Series I, b) Series II. The distributions were determined based on image analysis of SEM micrographs. Average grain diameters are indicated in each graph

## SUMMARY

This study presents a systematic investigation into the fabrication and optimization of functionally graded $Al_2O_3$-Ni ceramic metal composites using centrifugal gel casting with 2-carboxyethyl acrylate (CEA) as a novel polymerizable monomer. The research was driven by the need for structurally robust, thermally stable, and chemically resistant components for demanding industrial applications.

A key innovation lies in the use of CEA, whose carboxylic functionality enhances particle dispersion and electrostatic stability in aqueous suspensions. Compared to conventional acrylamide-based systems, the CEA-based formulation achieved superior homogeneity, reduced porosity, and high relative densities (>98%), marking a significant advancement in gel-casting chemistry for composite materials.

The study also highlights the critical role of centrifugal casting parameters in tailoring microstructural gradients. Two processing strategies Series I (high speed, short duration) and Series II (lower speed, longer duration) demonstrated distinct outcomes in particle redistribution and gradient formation. Series II, in particular, showed a more uniform nickel distribution and continuous metallic pathways across the sample cross-section, resulting in significantly improved compressive strength (1620.43 kN vs. 977.22 kN for Series I).

These findings confirm that both monomer chemistry and processing control are essential for achieving desirable microstructures and mechanical properties in functionally graded materials (FGMs). The ability to fine-tune phase gradients and enhance metal–ceramic integration opens new design possibilities for applications requiring a balance of hardness, toughness, and thermal resilience.

Ultimately, this work provides a practical and scalable approach for producing high-performance tubular ceramic–metal components. The combined insights into monomer selection, centrifugal processing, and microstructural engineering serve as a valuable foundation for future developments in FGMs for use in advanced piping systems, catalytic reactors, and energy-related modules operating under extreme conditions.

## ACKNOWLEDGEMENT

This publication was supported by grant No. TANGO-V-A/0004/2021 from the National Centre for Research and Development.

*Conflict-of-interest statement*

The authors certify that they have no affiliations with or involvement in any organization or entity with any financial interest, or non-financial interest in the subject matter or materials discussed in this manuscript.

## REFERENCES

1. Sun M., Ling Z., Mao J., Zeng X., Yuan D., Liu M.: Ammonia-Based Clean Energy Systems: A Review of Recent Progress and Key Challenges. *Energies* 18 (2025), 2845. https://doi.org/10.3390/en18112845

2. Abolore R.S., Jaiswal S., Jaiswal A.K.: Green and sustainable pretreatment methods for cellulose extraction from lignocellulosic biomass and its applications: A review. *Carbohydrate Polymer Technologies and Applications* 7 (2024), 100396. https://doi.org/10.1016/j.carpta.2023.100396.

3. Gouda A., Merhi N., Hmadeh M., Cecchi T., Santato C., Sain M.: Sustainable strategies for converting organic, electronic, and plastic waste from municipal solid waste into functional materials. *Global Challenges* 9 (2025), 2400240. https://doi.org/10.1002/gch2.20240024

4. Angelakis, A. N., Passchier, C. W., Valipour, M., Krasilnikoff, J. A., Tzanakakis, V. A., Ahmed, A. T., Baba, A., Kumar, R., Bilgic, E., Capodaglio, A. G., & Dercas, N. (2023). Evolution of Tunneling Hydro-Technology: From Ancient Times to Present and Future. Hydrology, 10(9), (2023), 190. https://doi.org/10.3390/hydrology10090190

5. Farh H.M.H., Ben Seghier M.E.A., Zayed T.: A comprehensive review of corrosion protection and control techniques for metallic pipelines. *Engineering Failure Analysis* 143 (2023), 106885. https://doi.org/10.1016/j.engfailanal.2022.106885.

6. Velasco D.C.R., Gonçalves V.P.D., Oliveira M.P., Simonassi N.T., Lopes F.P.D., Vieira C.M.F.: Industrial piping system: Design and corrosion protection. *Surfaces* 8 (2025), 18. https://doi.org/10.3390/surfaces8010018.
7. Waqar M., Memon A.M., Sabih M., Alhems L.M.: Composite pipelines: Analyzing defects and advancements in non-destructive testing techniques. *Engineering Failure Analysis* 157 (2024), 107914. https://doi.org/10.1016/j.engfailanal.2023.107914
8. Ali S., Wang X., Rasool G., Ali A., Ali R., ur-Rehman N., Razzaq I.: Theoretical study of the optical and thermodynamic properties of aluminum oxide ($Al_2O_3$) with high pressures at elevated temperatures. *Modern Physics Letters B* 39 (2025), 2350104. https://doi.org/10.1142/S0217984925501040.
9. Ruys A.: Alumina as a wear-resistant industrial ceramic. In: Ruys A. (Ed.), Alumina Ceramics, Woodhead Publishing Series in Biomaterials, Woodhead Publishing (2019), 369–411. https://doi.org/10.1016/B978-0-08-102442-3.00012-9.
10. Abyzov A.M.: Aluminum Oxide and Alumina Ceramics (review). Part 1. Properties of $Al_2O_3$ and Commercial Production of Dispersed $Al_2O_3$. *Refractories and Industrial Ceramics* 60 (2019), 24–32. https://doi.org/10.1007/s11148-019-00304-2
11. [11] Sun Y., Li S., Zhao Q., Cong Z., Xia Y., Jiao X., et al.: Recent Advancements in Alumina-Based High-Temperature Insulating Materials: Properties, Applications, and Future Perspectives. *High-Temperature Materials* 2 (2025), 10001. 10.70322/htm.2025.10001
12. Mohammed A.A., Khodair Z.T., Khadom A.A.: Preparation, characterization and application of $Al_2O_3$ nanoparticles for the protection of boiler steel tubes from high temperature corrosion. *Ceramics International* 46 (2020), 26945–26955. https://doi.org/10.1016/j.ceramint.2020.07.172
13. Smallman R.E., Bishop R.J.: Ceramics and glasses. Modern Physical Metallurgy and Materials Engineering, R.E. Smallman, R.J. Bishop, Butterworth-Heinemann, Oxford, 1999, 320–350.
14. Baudín C.: Alumina, Structure and Properties. Encyclopedia of Materials: Technical Ceramics and Glasses, M. Pomeroy, Elsevier, Amsterdam, 2021, 25–46.
15. Metson J.: Production of alumina. Fundamentals of Aluminium Metallurgy, R. Lumley, Woodhead Publishing, Cambridge, 2011, 23–48.
16. Hutsaylyuk V., Student M., Posuvailo V., Student O., Hvozdetskyi V., Maruschak P., Zakiev V.: The role of hydrogen in the formation of oxide-ceramic layers on aluminum alloys during their plasma-electrolytic oxidation. *Journal of Materials Research and Technology* 14 (2021), 1682–1696. https://doi.org/10.1016/j.jmrt.2021.07.082.
17. Hutsaylyuk V., Student M., Posuvailo V., Student O., Sirak Y., Hvozdetskyi V., Maruschak P., Veselivska H.: The properties of oxide-ceramic layers with Cu and Ni inclusions synthesizing by PEO method on top of the gas-spraying coatings on aluminium alloys. *Vacuum* 179 (2020), 109514. https://doi.org/10.1016/j.vacuum.2020.109514.
18. Zygmuntowicz J., Wiecińska P., Miazga A., Konopka K., Szafran M., Kaszuwara W.: Thermoanalytical studies of the ceramic-metal composites obtained by gel-centrifugal casting. *Journal of Thermal Analysis and Calorimetry* 133 (2018), 303–312. https://doi.org/10.1007/s10973-017-6647-z
19. Ruys A.: Processing, structure, and properties of alumina ceramics. In: Ruys A. (Ed.), Alumina Ceramics, Woodhead Publishing Series in Biomaterials, Woodhead Publishing (2019), 71–121. https://doi.org/10.1016/B978-0-08-102442-3.00004-X.
20. Piza M.M.T., Bergamo E.T.P., Campos T.M.B., Carvalho L.F., Goulart C.A., Gutierres E., Lopes A.C.O., Jalkh E.B.B., Bonfante E.A.: Alumina-toughened zirconia nanocomposite:

Aging effect on microstructural, optical, and mechanical properties. *Dental Materials* 39 (2023), 1022–1031. https://doi.org/10.1016/j.dental.2023.09.005.

21. Gogotsi G.A.: Fracture toughness of ceramics and ceramic composites. *Ceramics International* 29 (2003), 777–784. https://doi.org/10.1016/S0272-8842(02)00230-4

22. Rashid A.B., Haque M., Islam S.M.M., Labib U., Rafi K.M., Chowdhury P.: Breaking Boundaries with Ceramic Matrix Composites: A Comprehensive Overview of Materials, Manufacturing Techniques, Transformative Applications, Recent Advancements, and Future Prospects. *Advances in Materials Science and Engineering* (2024), 2112358. https://doi.org/10.1155/2024/2112358

23. Kota N., Charan M.S., Laha T., Roy S.: Review on development of metal/ceramic interpenetrating phase composites and critical analysis of their properties. *Ceramics International* 48 (2022), 1451–1483. https://doi.org/10.1016/j.ceramint.2021.09.232

24. Faber K.T.: Ceramics: Microstructural Toughening (Excluding Transformation Toughening, Whisker Toughening, and Continuous Fiber Toughening). Encyclopedia of Materials: Science and Technology, K.H.J. Buschow et al., Elsevier, Amsterdam, 2001, 1108–1112.

25. Van Mier J.G.M.: Concrete: Failure Mechanics. Encyclopedia of Materials: Science and Technology, K.H.J. Buschow et al. , Elsevier, Amsterdam, 2001, 1479–1482.

26. Silva R.F., Coelho P.G., Gustavo C.V., Almeida C.J., Farias F.W.C., Duarte V.R., Xavier J., Esteves M.B., Conde F.M., Cunha F.G., et al.: Functionally graded materials and structures: Unified approach by optimal design, metal additive manufacturing, and image-based characterization. *Materials* 17 (2024), 4545. https://doi.org/10.3390/ma17184545.

27. Aboudi J., Pindera M.-J., Arnold S.M.: Higher-order theory for functionally graded materials. *Composites Part B: Engineering* 30 (1999), 777–832. https://doi.org/10.1016/S1359-8368(99)00053-0.

28. Li Y., Feng Z., Hao L., Huang L., Xin C., Wang Y., Bilotti E., Essa K., Zhang H., Li Z., Yan F., Peijs T.: A review on functionally graded materials and structures via additive manufacturing: From multi-scale design to versatile functional properties. *Advanced Materials Technologies* 5 (2020), 1900981. https://doi.org/10.1002/admt.201900981.

29. Saleh B., Jiang J., Fathi R., Al-hababi T., Xu Q., Wang L., Song D., Ma A.: 30 Years of functionally graded materials: An overview of manufacturing methods, applications and future challenges. *Composites Part B: Engineering* 201 (2020), 108376. https://doi.org/10.1016/j.compositesb.2020.108376.

30. Sharma N.K., Bhandari M.: Applications of functionally graded materials (FGMs). *International Journal of Engineering Research & Technology (IJERT)* 2 (2014), 2.

31. Silva R.F., Coelho P.G., Gustavo C.V., Almeida C.J., Farias F.W.C., Duarte V.R., Xavier J., Esteves M.B., Conde F.M., Cunha F.G., Santos T.G.: Functionally Graded Materials and Structures: Unified Approach by Optimal Design, Metal Additive Manufacturing, and Image-Based Characterization. *Materials* 17 (2024), 4545. https://doi.org/10.3390/ma17184545

32. Mohammadi M., Rajabi M., Ghadiri M.: Functionally graded materials (FGMs): A review of classifications, fabrication methods and their applications. *Processing and Application of Ceramics* 15 (2021), 319–343. 10.2298/PAC2104319M

33. Zygmuntowicz J., Wiecińska P., Miazga A., Konopka K., Kaszuwara W.: $Al_2O_3$/Ni functionally graded materials (FGM) obtained by centrifugal-slip casting method. *Journal of Thermal Analysis and Calorimetry* 130 (2017), 123–130. https://doi.org/10.1007/s10973-017-6232-5

34. Kausar A.: Progress in Polymer Nanocomposites for High-Performance Applications. *Polymer-Plastics Technology and Materials* 62 (2023), 453–472.

35. EN 623–2: Advanced technical ceramics – Determination of density and porosity, 1993.

36. Kurzydłowski K.J., Ralph B.: The Quantitative Description of the Microstructure of Materials. CRC Press, Boca Raton, 1995.

37. Wejrzanowski T., Spychalski W., Rożniatowski K., Kurzydłowski K.J.: Image based analysis of complex microstructures of engineering materials. *International Journal of Applied Mathematics and Computer Science* 18 (2008), 33–39. 10.2478/v10006-008-0003-1

38. Michalski J., Wejrzanowski T., Pielaszek R., Konopka K., Łojkowski W., Kurzydłowski K.J.: Application of image analysis for characterization of powders. *Materials Science-Poland* 23 (2005), 79–86.

39. Wejrzanowski T., Kurzydłowski K.J.: Stereology of grains in nano-crystals. *Solid State Phenomena* 94 (2003), 221–228. 10.4028/www.scientific.net/SSP.94.221

40. Pietrzak E., Wiecińska P., Szafran M.: 2-carboxyethyl acrylate as a new monomer preventing negative effect of oxygen inhibition in gelcasting of alumina. *Ceramics International* 42 (2016), 13682–13688. https://doi.org/10.1016/j.ceramint.2016.05.166

41. Zygmuntowicz, J., Kosiorek, M., Piotrkiewicz, P., Wachowski, M., Szachogłuchowicz, I., Kaszuwara, W., Konopka, K., Falkowski, P., & Piątek, M.: Gradient composites $Al_2O_3$–Ni obtained via the CSC technique in a magnetic field. *Journal of Alloys and Compounds. Advance* 1008 (2024), 176532. https://doi.org/10.1016/j.jallcom.2024.176532.

42. González C., Segurado J., Llorca J.: Numerical simulation of elasto-plastic deformation of composites: evolution of stress microfields and implications for homogenization models, *Journal of the Mechanics and Physics of Solids*, 52, 7, (2004), 1573-1593, https://doi.org/10.1016/j.jmps.2004.01.002.

43. Wu, H., Xu, W., Shan, D., Wang, X., Guo, B., Jin, B.C.: Micromechanical modeling of damage evolution and fracture behavior in particle reinforced metal matrix composites based- on the conventional theory of mechanism-based strain gradient plasticity. *J. Mater. Res. Technol*. 22, (2023) 625–641.

44. Périé J.-N., Passieux J.-Ch.: Advances in Digital Image Correlation (DIC). *Applied Sciences*, 2020. 10.3390/books978-3-03928-515-0.